Journal of Photochemistry & Photobiology, A: Chemistry 453 (2024) 115653

Contents lists available at ScienceDirect

Journal of Photochemistry & Photobiology, A: Chemistry

journal homepage: www.elsevier.com/locate/jphotochem

Immobilisation of ZnO nanoparticles on carbon and on glass fibres for visible light photocatalytic applications

Inês V. Ferreira [a], Nuno R. Neng [a,b], Olinda C. Monteiro [a], Virgínia C. Ferreira [a,*]

[a] Centro de Química Estrutural, Institute of Molecular Sciences, Faculdade de Ciências, Universidade de Lisboa, Campo Grande, 1749-016 Lisboa, Portugal
[b] Laboratório de Ciências Forenses e Psicológicas Egas Moniz, Egas Moniz Center for Interdisciplinary Research, Egas Moniz School of Health & Science, Quinta da Granja, 2829-511 Caparica, Almada, Portugal

ARTICLE INFO

Keywords:
Metal-doping
Supported nanocatalysts
Fibre-based composites
Photocatalytic degradation
Pharmaceutical drugs

ABSTRACT

Crystalline zinc oxide (ZnO) nanoparticles (NP) have been used for the evaluation of the effect of manganese doping on the photocatalytic performance towards the degradation of pharmaceutical products and for the preparation of photoactive composite materials based on fibres and ZnO.

The presence of manganese effected on the particles size, as obtained by TEM analysis, and the impact on the crystallographic and optical properties was shown by XRD and DRS analysis. The multiple oxidation state of the doping manganese and its impact on the oxygen vacancies of the material, together with possibility of introducing energy levels in the forbidden zone and changes in the bandgap energy could contribute to improve the catalyst properties. However, and contrasting with some reported works, no advantage using the doped particles was observed on the photocatalytic response under UV or visible light irradiation.

Later, the ZnO NP were immobilised by *in situ* hydrothermal approach on carbon and glass fibres and the composites show good nanoparticles coverage on the SEM images and the EDS, FTIR and DRS data are consistent with the presence of NP on the surfaces. Those composites have been successfully used for the degradation of the Diclofenac (DCF) and Carbamazepine (CMZ) pollutants. The complexity of the photodegradation under UV and visible light, due to the production of absorbing degradation products, was unveiled by UV–vis spectroscopy and HPLC analysis, and showed that distinct products may be detected during degradation, depending on the radiation used. The photostability of ZnO nanoparticles and the CF/ZnO composite maintaining 83 % of its initial efficiency after three cycles of reuse highlight the method's success in supporting nanoparticles on substrates and demonstrates promising applicability in fields such as environmental remediation.

1. Introduction

The water shortage and environmental pollution is a major issue across the globe and has significant impact in our health and daily life. Therefore, the development of effective approaches for pollutants removal from wastewater is of major concern. Technologies based on adsorption and advanced oxidation processes (AOP), such as photo (electro)catalysis, have been intensively exploited to this purpose [1,2]. The use of photoactive catalysts has shown important advances and promising results. The photocatalysts may include metal oxides [3–6], chalcogenides [7,8], oxyhalides [5,9,10] and other [11,12], and many allow the degradation, by photo-assisted oxidation processes, of contaminants such as dyes and pharmaceutical products within minutes using small amount of catalyst.

Among the most investigated semiconductor catalysts are titanium dioxide (TiO_2) and zinc oxide (ZnO), which have been used namely in biomedical, (photo)catalytic, UV shielding and photovoltaic applications [1,2]. ZnO is a direct semiconductor with bandgap energy of ca. 3.37 eV and has been proposed as an alternative to TiO_2 photocatalyst due to its higher absorption efficiency [4,13,14]. The ZnO's *hexagonal wurtzite* phase is the most stable and it can be obtained by mild hydrothermal conditions [4,15]. One of the ZnO's main drawback for photocatalytic applications is its low charge separation efficiency and photocorrosion. To overcome such problem, several approaches have been reported in the literature, including metal and non-metal doping and the production of composite materials. Qamar *et al.* [5] reported the doping of ZnO with transition metals (Fe, Co, Ni, Mn and Cr). The presence of the metal introduces energy levels in the forbidden zone decreasing the

* Corresponding author.
E-mail address: vcferreira@fc.ul.pt (V.C. Ferreira).

https://doi.org/10.1016/j.jphotochem.2024.115653
Received 19 December 2023; Received in revised form 27 March 2024; Accepted 31 March 2024
Available online 5 April 2024

electron/hole (e^-/h^+) recombination and improving the antibacterial and photocatalytic activity under sunlight. Manganese is a good candidate for doping since it can lower bandgap energy and add intermediate bands in the forbidden zone, facilitating multi-band optical absorption [16]. Moreover, Mn-doping can also increase the oxygen vacancies concentration [17,18], promote multiple charge transfer pathways due to its multi-oxidation states, and create the opportunity to ally photocatalysis to (photo)Fenton-like processes in nanomaterials, as it has been described for Mn-CeO_2 [19], Mn-TiO_2 [20] and Mn-Titanates [16,21]. It has also been reported that doping with non-metals, such as N, C or S, may prevent the recombination of the e^-/h^+ pairs by acting as electron scavengers [6,13]. Another successful approach used to improve the ZnO properties, namely its activity under visible light, is the preparation of ZnO hybrid materials. Examples are those hybrids with MnO, BiOCl and TiO_2 [10,14,22–24]. The visible light active photocatalysts are highly desirable since those are more easily activated and can be used under less energetic, widely available and inexpensive radiation sources.

The use of powdered photocatalysts poses some challenges, mostly to their recovery and multi-cycle use, and possible inadvertent release to the environment. Therefore, several approaches have been used to immobilise the nanocatalysts on surfaces, such as dip-coating, solvent-casting, spray coating or *in situ* modification through the impregnation of reactants followed by the synthesis step [9,25–28]. The substrates can include textiles and fibres (base for the development of self/cleaning fabrics), glass, polymers (*e.g.* polydimethylsiloxane - PDMS), metal and many other. The *in situ* one-pot synthesis approach has the advantage of allowing the growth of the nanocatalysts directly on the substrate surface, enhancing the stability and favouring the interaction at the nanoparticles/substrate interface. Franco *et al.* [29] reported that although immobilised ZnO and Cd-doped ZnO nanoparticles on glass show lower efficiency (75 %) for the degradation of methylene blue dye (MB) as compared with powder samples, it has the advantage of easy recovery of the catalyst. Kim *et al.* [30] showed that ZnO immobilised on a polymeric polyurethane membrane assisted by a polydopamine layer enables the efficient removal of MB. Also, ZnO immobilised on natural fibres and BiOCl and TiO_2 on cotton fibres enabled the repeatedly removal of Congo Red and Naphthol Blue Black dyes, respectively, from aqueous solutions [31,32].

In this work, the preparation and the structural, morphological, optical and photocatalytic characterisation of pristine and Mn-doped ZnO nanoparticles is reported. The changes due to Mn addition are investigated to assess the ability of these nanoparticles to efficiently use visible light, with special focus on photocatalytic applications. Pursuing our interest in composite materials, the best catalyst immobilised on fibres (carbon and glass) are characterised and the photocatalytic performance assessed towards the degradation of pharmaceutical products, Diclofenac and Carbamazepine, envisaging the application under visible light irradiation.

2. Experimental details

2.1. Reagents and materials

All reagents were of analytical grade and used as received. Distilled water was used for solutions preparation. Glass (GF) and carbon (CF) fibres were purchased from Quimer – Produtos Químicos, Lda (Portugal), previously washed with propan-2-ol for 30 min and dried in the oven at 55 °C.

2.2. Nanoparticles synthesis

The crystalline ZnO nanoparticles synthesis was performed according to the procedure published elsewhere [4]. Briefly, 2 mmol of zinc acetate, $Zn(CH_3CO_2)_2{\cdot}2H_2O$, were dissolved in 30 mL of ethanol and 2.05 mmol of sodium hydroxide, NaOH, were dissolved in another 30 mL of ethanol. The NaOH solution was added dropwise to the zinc solution at room temperature under stirring. At the end, the stirring was maintained for additional 30 min. The solution was transferred to an autoclave and heated in the oven for 24 h at 160 °C. Later, the resulting nanoparticles in suspension were washed twice with water and once with ethanol, and collected by centrifugation. The solid was dried in the oven and stored.

The Mn-doped ZnO nanoparticles were prepared by the same method, by adding the desired amount of manganese, as manganese acetate ($Mn(CH_3CO_2)_2{\cdot}4H_2O$), to the synthesis solution, according to the procedure reported in the literature [1]. In this case, the nominal amount of Mn used was 1 and 3 % (0.02 and 0.06 mmol, respectively). The Mn-doped nanoparticles, Mn(1%)ZnO and Mn(3%)ZnO, were washed, collected, dried and stored.

Titanium dioxide, TiO_2, nanoparticles were used only for comparison purposes and have been prepared according to a 2-step method described in the literature [31]. An amorphous precursor was prepared by precipitation reaction, by adding, dropwise and under stirring, ammonium hydroxide (NH_4OH) solution to the titanium trichloride ($TiCl_3$) solution in hydrochloric acid (HCl). After washing and collecting the precursor by filtration, it was added to an autoclave with distilled water and heated at 200 °C for 6 h. The crystalline TiO_2 nanoparticles were washed trice with distilled water, collected, dried and stored.

2.3. Fibres modification with nanoparticles

The fibres modification with pristine and Mn-doped ZnO nanoparticles was performed *in situ* as described above for the particle's synthesis, in the presence of 1.5 g of fibres (CF or GF) per batch of synthesis.

2.4. Characterization of materials

The X-ray powder diffraction (XRD) analysis of powder and fibre samples was carried out in a Philips X-ray diffractometer (PW 1730 and automatic data acquisition APD Philips v3.6B), with Cu Kα radiation ($\lambda = 0.15406$ nm) and at 40 kV/30 mA. The diffraction patterns were collected in the range of $2\theta = 20–80$ ° with a 0.02 ° step size and 100 s per step acquisition time. The UV–vis analysis of liquid samples was performed in a Shimadzu UV-2600PC spectrophotometer, between 200 and 600 nm, using 1 cm path quartz cuvettes; the diffuse reflectance spectroscopy (DRS) spectra of nanoparticles and modified fibres were obtained using the same equipment with an ISR 2600plus integration sphere. The spectra were recorded between 200 and 1400 nm, using barium sulphate powder as reference standard. Transmission electron microscopy (TEM) analysis and selected area electron diffraction (SAED) were performed using a JEOL 200CX microscope operating at 200 kV with the powder samples supported on copper grids. Scanning electron microscopy (SEM) analysis was obtained using a Thermo Scientific Phenom PROX G6 microscope with EDS analysis, using a combination of secondary and backscattered electrons and operating at 15–20 kV. Fourier Transform Infra-Red Spectroscopy (FTIR) analysis was performed in a Nicolet 6700 spectrophotometer from Thermo Electron Corporation between 400 and 4000 cm^{-1} using KBr pellets for powder samples. The specific surface area was measured by the Brunauer-Emmett-Teller (B.E.T.) method, in the same conditions as previously reported [9,31]. Atomic absorption spectroscopy analysis (AAS) was performed in an Analytik Jena spectrophotometer, model novAA 350, using an acetylene/air mixture. The samples were previously digested in HNO_3 and filtrated for fibres removal.

2.5. Photocatalytic degradation of pollutants

The photocatalysis experiments were conducted using: (i) UV and visible light using a Hanovia medium pressure mercury-vapor lamp (450 W) in a 250 mL refrigerated quartz photoreactor [9,31], from here on referred to as UV, and (ii) visible light using an Oriel 300 W Xenon

lamp in a borosilicate glass reactor (acting as an UV filter) positioned at ca. 30 cm from the sample [31], from here on denoted as Vis. The catalyst sample, 20 mg of powder NP catalyst (250 mg if using fibre-NP sample), was suspended in 150 mL of the pollutant solution (DCF or CMZ, 10 ppm) and stirred in dark conditions for 30 min to allow the adsorption/desorption equilibrium. After this time, prior to irradiation, an aliquot of solution was collected to evaluate the adsorption of the pollutant on the catalyst surface and used as t = 0 for the photocatalytic degradation. During irradiation, aliquots of the suspensions were collected at regular intervals, centrifuged and first analysed by UV–vis spectroscopy. Reutilisation cycles of ZnO and CF/ZnO were performed in CMZ solution for 1 and 3.5 h runs, respectively, after which time the absorption peaks of CMZ still allows its detection by UV–vis spectroscopy.

High-performance liquid chromatography was performed with a diode array system, HPLC-DAD, from Agilent Technologies, Germany, with detection at 278 nm. The data acquisition and instrument control used the software LC3D ChemStation (version Ver.A.10.02.1757; Agilent Technologies, Germany). The chromatographic separation was achieved in a column Kinetex C18 (150 x 4.6 mm, 2.6 μm particle size; Phenomenex, EUA) at 20 °C. The sample (20 μL) was eluted with a solution 55:45 (DCF) and 30:70 (CMZ) acetonitrile/2.5 % acetic acid aqueous solution, with a flow of 0.6 mL/min.

3. Results and discussion

3.1. Structural, optical and morphological characterisation of the nanoparticles

Crystalline ZnO and Mn-doped ZnO NP (1 and 3 % of manganese nominal content) have been successfully obtained as illustrated in Fig. 1a. The XRD pattern shows sharp and narrow diffraction peaks for all the samples, corresponding to the hexagonal *wurtzite* structure of ZnO (ICCD PDF file 36-1451). A small shift was observed in the 2θ values of the diffraction peak at 36.253 ° (Fig. 1b) for the Mn-doped samples, and the values are included in Table 1. A shift towards lower 2θ values in the Mn(1 %) sample has been assigned to the presence of larger Mn^{2+} ions (0.66 Å) in the ZnO structure, as compared with Zn^{2+} (0.60 Å). Whereas the shift towards higher values, for 3 % Mn nominal content in Mn-doped ZnO, has been ascribed to the content of smaller Mn^{3+} ions (0.58 Å) [15]. In fact, Lu *et al.* [15] reported that Mn^{2+}/Mn^{3+} species coexists in ZnO and that as the Mn-doping increases from 1 to 5 %, a concomitant increase of Mn^{3+} is observed, as compared with Mn^{2+}. Apart from other implications, such as creating intermediate bands in the forbidden zone and affect the bandgap energy, depending on the oxidation state of the Mn, it can have impact in the oxygen vacancies of the material [17,18].

The decrease in intensity and widening of the diffraction peaks with doping suggests the decrease in the nanometric particle size, confirmed by TEM analysis, Fig. 1b-d, in agreement to the variation previously reported [4,38]. This may arise from the distortions in the crystal owing to the incorporation of Mn ions in the crystalline structure constraining the particles growth, as suggested in literature [15,33]. In fact, it has been reported, for Mn-doped ZnO nanoparticles prepared by several methods, including solvothermal method used in this study, that the doping occurs with incorporation of Mn atoms in the crystalline structure of ZnO, replacing Zn atoms [15,18,34]. The amount of doping ion is expected to be within the solubility limit and no peaks assigned to any Mn_xO_y crystalline phase were detected in this work in the XRD pattern of the doped ZnO NP [35].

To further confirm this, a sample with a large excess of Mn (30%) was prepared, Mn(30%)ZnO. Here, the detection of diffraction peaks at 2θ values about 29.4, 33.1, 59.0, 60.9 and 65.2 ° (ESI, Figure S2) can be ascribed to the $ZnMn_2O_4$ spinel (JCPDS 24–1133) [35–37]. These were not detected on the Mn-doped samples prepared in this work.

The TEM images in Fig. 2 show the presence of spherical and ellipsoid ZnO NP with average size of 21 ± 5 nm. As the manganese nominal content increases, the NP size decreases, Table 1, and for the Mn(3%)ZnO sample, small 12 ± 2 nm spherical particles are observed. Their crystallinity was further confirmed by SAED analysis (Insets in Fig. 2 (a-c)).

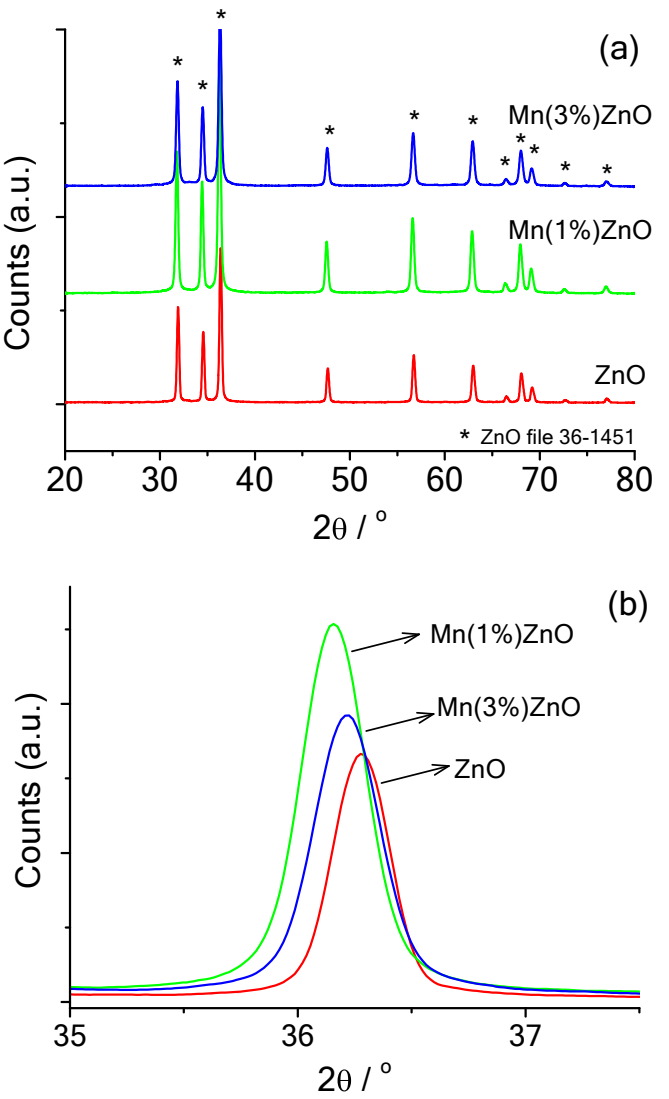

Fig. 1. (a) Full XRD powder diffraction patterns of pristine and Mn-doped ZnO NP (1 and 3 % of manganese) and (b) detail of diffraction peak at 36.25 °.

Table 1
Characterisation parameters of the pristine and Mn-doped ZnO particles, XRD peak shift, TEM particle size, B.E.T. surface area and bandgap energy, E_g.

Sample	2θ shift / ° (@ 36.253 °)	Particle size / nm	Surface Area / m^2/g	E_g / eV
ZnO	–	21 ± 5	26.2	3.28
Mn(1%)ZnO	−0.117	17 ± 3	23.8	3.30
Mn(3%)ZnO	−0.061	12 ± 2	19.0	3.29

The optical characterization of the prepared powder samples was performed by diffuse reflectance spectroscopy. The Kubelka-Munk function, F_{KM}, is correlated to the reflectance (R) according to equation (1) and is proportional to the absorption coefficient. In Fig. 3 are the F_{KM} absorption spectra of the samples. The bandgap energy, E_g, for the prepared samples, included in Table 1, were obtained from the Tauc plots for direct transitions (ESI, Figure S3), by plotting f_{KM} *vs* energy, hν, according to equation (2) [7,31].

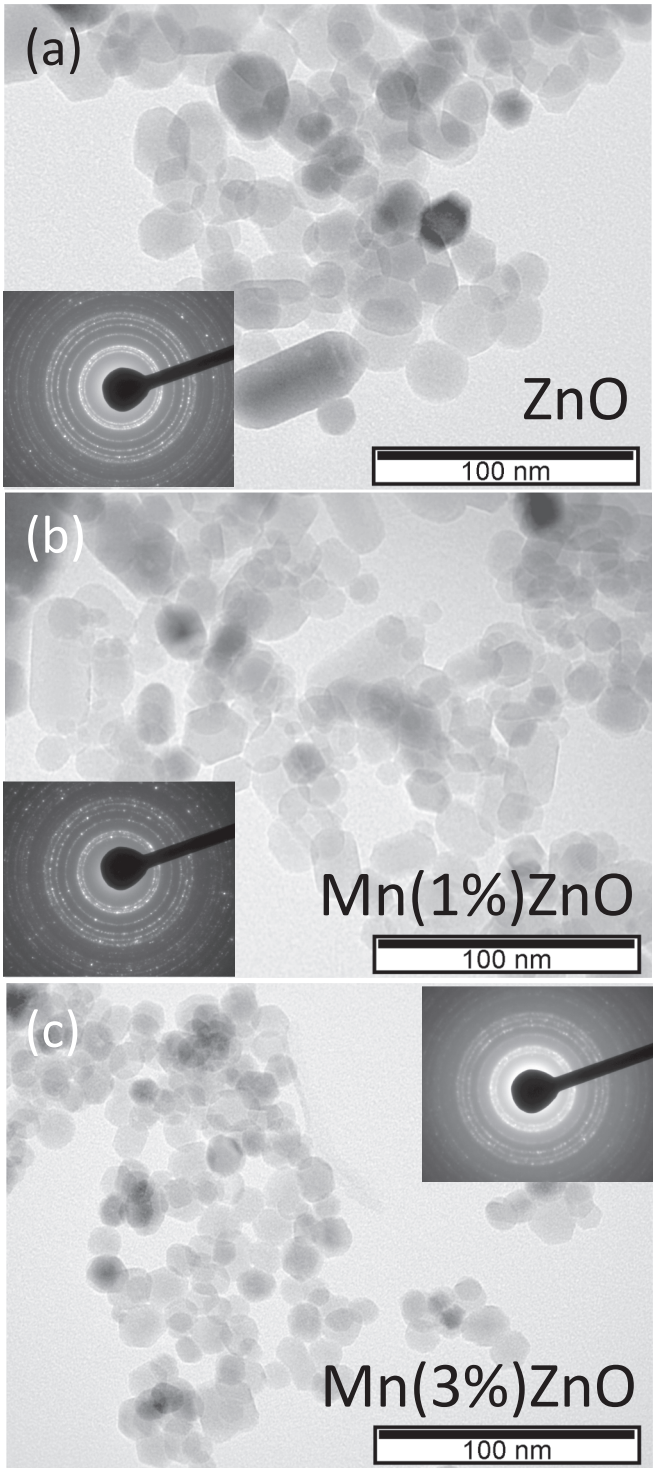

Fig. 2. TEM images of (a) pristine ZnO NP and (b, c) doped with 1 and 3 % of manganese. Inset: SAED images of the corresponding samples.

$$F_{KM} = \frac{(1-R)^2}{2R} \quad (1)$$

$$f_{KM} = (F_{KM} h\nu)^2 \quad (2)$$

Although the DRS spectra of the Mn-doped ZnO NP (Fig. 3) suggests the change in the nanoparticle's absorption upon doping, the bandgap energy of the semiconductor does not change for the doping level used in this work, Table 1. In fact, variation could be expected due to several

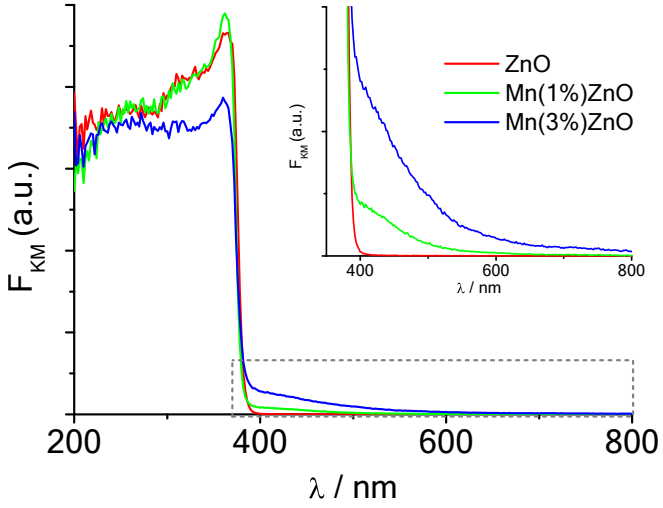

Fig. 3. F_{KM} absorption spectra of pure and Mn-doped ZnO samples.

factors. First, a decrease in the particles size could result in an increase of E_g due to quantum confinement. Second, the formation of new energy levels between the valence and the conduction bands upon doping of semiconductor NP, resulting in the decrease of e^-/h^+ recombination. In fact, contrasting results have been reported, namely by Wang *et al.* [22] who observed a small red shift (-0.05 eV) for 5 % Mn doping on ZnO prepared by electrospinning, whereas Toufic *et al.* [38] and *Lu et al.* [15] observed a bandgap increase (blue shift) for pure ZnO and Mn(6% & 5%) ZnO, respectively, in samples prepared by hydrothermal method. Also, in Mn-doped ZnO films prepared by laser deposition [39] the E_g decreased for 1 % Mn and increased from thereafter up to 10 % of doping. In this case, only an absorption extended to a wide range of wavelength above the absorption edge was observed. This has been assigned to the charge–transfer transition between donor and/or acceptor ionization levels of Mn ions and the band continuum, rather than to discrete forbidden *d-d* transitions [40].

The surface area of the nanoparticles was measured by nitrogen adsorption isotherms through the B.E.T. method, which values are included in Table 1. Although the particle size decreases with the Mn content, the specific surface area also seems to decrease. A more detailed analysis of the nitrogen adsorption isotherms recorded for the surface area measurement (ESI, Figure S4) suggest the absence of pores in the prepared NP and although the external surface area did not increase as the particles size decreases, the total volume within the finely divided powder in the smaller Mn-doped particles is higher than that of bigger undoped ZnO (8 and 6 mm^3/g, respectively, at maximum pressure). Therefore, the decrease of the surface area with doping may be attributed to the high degree of particles aggregation [41].

By FTIR analysis (ESI, Figure S5) and according to literature [42–44], it was possible to identify, for the powder NP, a broad absorption band centred at 3500 cm^{-1} corresponding to the stretching vibration of the O-H of H_2O (1); at 2924 (strong absorption band) and at 2852 cm^{-1} stretching bands of C-H bond (2); the bands at ca. 2347–2372 cm^{-1} correspond to CO_2 from air (3). Stretching vibration bands of C-H at 1373 and 1437 cm^{-1} (4); between 835 and 1080 cm^{-1} are the angular bending bands of carbonate and the stretching band of C-O assigned to the zinc acetate (5). The band at about 1219 cm^{-1} may be assigned to the symmetric deformation of the O-H bond. In the range between 704 and 607 cm^{-1} are observed strong stretching bands in the ZnO NP (6) and at wavenumber below 580 cm^{-1} is the characteristic band of the stretching vibration of the Zn-O bond (7). A more detailed analysis showed that a small shoulder at 457 cm^{-1}, characteristic of the stretching of ZnO, shifts towards higher frequency with increasing Mn content in the crystalline structure, to 486 and 490 cm^{-1} for samples Mn (1%)ZnO and Mn(3%)ZnO, respectively, in agreement with the

literature [45].

3.2. Photocatalytic characterisation of nanoparticles

In this work, the two model pollutants, Diclofenac and Carbamazepine, have been used for the study of the photocatalytic activity of ZnO and Mn-ZnO crystalline nanocatalysts under visible light (Vis), and for its performance when immobilised *in situ* on fibres.

The nanocatalysts have been preliminarily tested under UV radiation for initial screening. In Fig. 4 are represented the time profiles for the CMZ degradation under visible radiation using pristine and Mn-doped samples. The best performance was achieved for pure ZnO NP. No advantages have been found in doping the ZnO NP with manganese on the photocatalytic degradation of either CMZ under visible light, as illustrated in Fig. 4, or DCF under UV–visible or visible light irradiation (ESI, Figure S6). The better photocatalytic response of ZnO may have the contribution of the higher surface area of those particles, Table 1, and therefore, it was selected for further studies.

The typical UV–vis spectra for DCF and CMZ aqueous solutions during degradation under UV radiation are illustrated in ESI, Figure S7. DCF is an anionic molecule with pK_a of 4.2 [46] displaying an absorption band at about 276 nm. In the presence of the pristine ZnO catalyst, under UV radiation, DCF undergoes degradation (ESI, Figure S7a). The complex specta obtained during irradiation, displays absorption bands namely at about 202, 216, 240, 279 and 288 nm, reflects the formation of absorbing degradation products. Comparable results are obtained for the degradation products under UV and Vis radiation (ESI, Figure S8). It has been reported in literature that such products can include pyrocatechol, 2-aminophenol, 2,6-dichloroaniline and 2,6-dichlorophenol which show several absorption bands between 200 and 290 nm [46].

On the other hand, CMZ is a neutral molecule with pK_a of 13.9 [47]; it is used as an anticonvulsant drug. Its photodegradation under UV radiation, using the ZnO nanoparticles as catalyst, are shown in ESI, Figure S7b. The comparison between the time profiles obtained from the UV–vis (at $\lambda = 285$ nm) and HPLC data, depicted in Fig. 5 for UV and for Vis light irradiation, show that the CMZ is faster degraded than suggested by a simple UV–vis analysis. The % of removal detected was 100 and 81 % by UV–vis and HPLC analysis, respectively, under UV irradiation and 49 and 29 % under Vis irradiation at t = 20 min. That is due to the formation of degradation products that also absorb in the UV and visible range, interfering with the quantification. Therefore, the CMZ concentration values obtained by UV–vis spectroscopy are

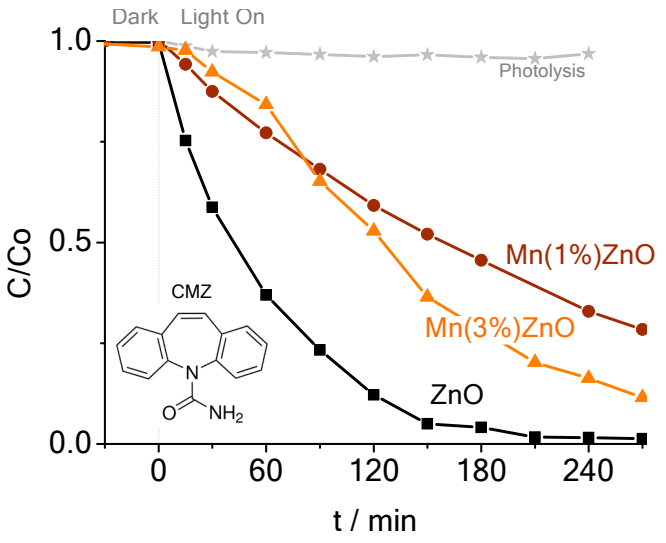

Fig. 4. Time profiles for the degradation of CMZ (10 ppm; 150 mL) with pristine and manganese doped ZnO NP under visible light irradiation and comparison with photolysis.

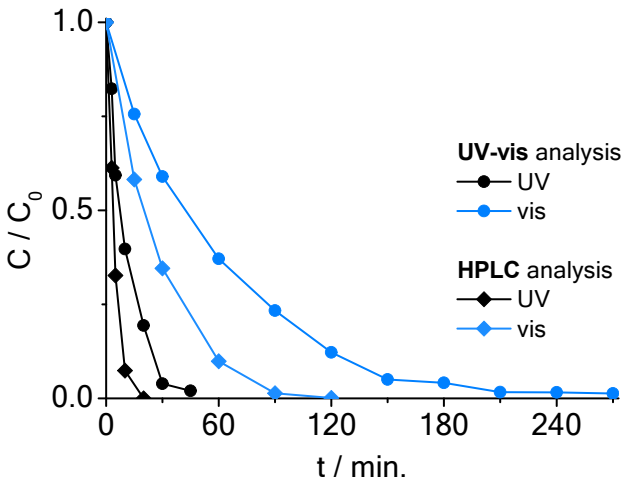

Fig. 5. Time profiles for the degradation of CMZ (10 ppm; 150 mL) under UV and under Vis light irradiation, with ZnO NP catalyst (20 mg), obtained from UV–vis spectroscopy and HPLC analysis.

overestimated. CMZ degradation products have been reported in the literature as including hydroxy and keto derivatives, epoxidation, deamidation and heterocycle-ring opening products and lower molecular weight molecules [12,48,49].

A more detailed analysis of the HPLC data obtained for the photocatalytic removal of CMZ with ZnO NP under UV and under Vis radiation (retention time of CMZ, t_R = 10.90 min), shows that most of the degradation products occur independent on the radiation used (ESI, Figure S9). However, the speed of formation and/or degradation of such products depends on the radiation energy and therefore some of them are only detected under Vis radiation (in some cases in a large extent) such as those at t_R = 2.51, 2.90, 4.56, 5.15, 5.24 and 5.86 min, whereas other products are only detected under UV radiation (t_R = 2.69, 3.22, 3.41, 3.72, 4.05, 4.39 and 4.73 min). These results suggest, as expected, that degradation under lower energy radiation is slower and allows the accumulation of species and its detection by HPLC.

Under visible light, the catalyst retains the full capacity for CMZ degradation, since for the ZnO NPs, no activity loss due to surface blocking or photo-corrosion was observed over 5 reutilisation cycles (ESI, Figure S10). The CMZ degradation ratio still reaches 83 % of the initial 63 %, after 5 cycles, indicating the good reusability and high stability of ZnO nanoparticles. Also, XRD analysis, detailed in ESI, Figure S11, shows that ZnO sample remains stable and with unchanged crystalline structure before and after photocatalysis, after which no new phases or degradation was observed.

The performance of pristine ZnO NP was contrasted with that of crystalline 12 nm TiO_2 *anatase* NP (ESI, Figure S12). ZnO has shown a better performance than a synthesised TiO_2 nanoparticles sample (*anatase* phase) for the degradation of DCF and CMZ, and a complete removal of the pollutants and absorbing degradation products is observed in Fig. 6 after 30–45 min of irradiation with UV light. This effect cannot be regarded as a surface area effect since TiO_2 has a 3-fold higher area than ZnO (75.0 and 26.2 m^2/g, respectively), neither from the band gap energy which is similar for both materials (3.26 and 3.24 eV, respectively), Table 1. Also, considering the similar valence band energy of TiO_2 and ZnO reported in the literature [24], it should not be the case. The better photocatalytic performance of ZnO as compared with TiO_2 has been ascribed to the higher mobility of ZnO's electrons, which enhances the electron transfer, imparting high quantum efficiency [13].

Due to the excellent performance of pure ZnO towards the photocatalytic degradation of the pollutants, the study proceeded with those particles immobilised on fibres. The carbon and glass fibres were chosen

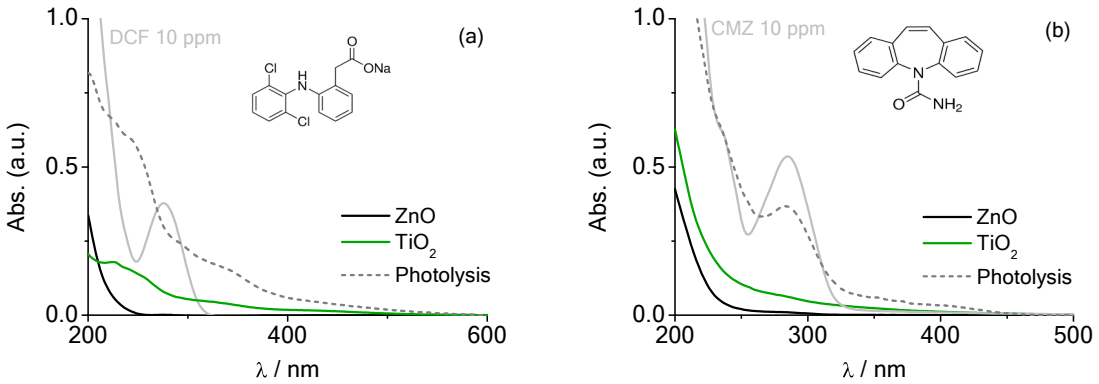

Fig. 6. UV–vis spectra for the degradation of (a) DCF at t = 30 min and (b) CMZ at t = 45 min, by ZnO and TiO_2 NP under UV radiation and comparison with photolysis; DCF and CMZ initial concentration: 10 ppm.

due to their stability, ease of manipulation and availability.

3.3. Characterisation of Fibre/ZnO composites

The SEM images in Fig. 7 and Fig. 8 confirm the successful *in situ* immobilisation of the ZnO NP on the glass and carbon fibres, respectively, as a layer of material can be clearly distinguished on the surface as compared with the clean fibre. Also, the qualitative elemental analysis by EDS along the line scan in Fig. 7(c,d) (spectra in the inset), shows the change in Zn and Si content (for GF) and C (for CF) in Fig. 8(c,d), as the scan moves from a scratched or less covered surface (exposed substrate) to highly ZnO coated areas. These results show a uniform and stable coating of ZnO on both substrates.

The diffuse reflectance spectra of GF/ZnO samples, shown in Fig. 9, corroborates the presence of ZnO nanoparticles on the GF surface with a steep reflectance drop at 385 nm and a shoulder between 320 and 370 nm not observed in the GF spectrum. Due to the black colour of the carbon fibres and their high absorbance in the whole UV and visible range it was not possible to detect the presence of the NP on CF by DRS analysis.

The FTIR characteristic absorption bands supports the SEM results and confirm the presence of ZnO on CF. Thus, on CF/ZnO (ESI, Figure S13a) the absorption bands at about 3600–3850 cm^{-1}, 2900 cm^{-1}, 1700 cm^{-1}, 1518 cm^{-1} and 676 cm^{-1} have been assigned to O-H stretching vibrations of adsorbed hydroxyl groups and H_2O (1), C-H stretching of $–CH_2$ and $–CH_3$ (2), C=O of carbonyl or ketone groups (3), C=C carbon backbone (4) and C-H bending (5), respectively [50], whereas on GF/ZnO (ESI, Figure S13b), absorption bands at 3500 cm^{-1}, 2924 and 2852 cm^{-1}, 1830 cm^{-1}, 1450 cm^{-1}, 1260 cm^{-1} and 960–1020 cm^{-1} have been assigned to stretching vibrations of O-H from H_2O and Si-OH (1), to C-H (2) and C=O (3), bands characteristic of oxides (4), Si-C (5) and Si-O-Si (6), respectively [51,52]. Upon modification with ZnO, on CF/ZnO the occurrence of the intense absorption band centred at 524 cm^{-1} (6) can be assigned to the presence of ZnO on the fibre surface according to the previously discussed for ZnO NP [38,44]. On the other hand, it was not detected any feature ascribable to the presence of the

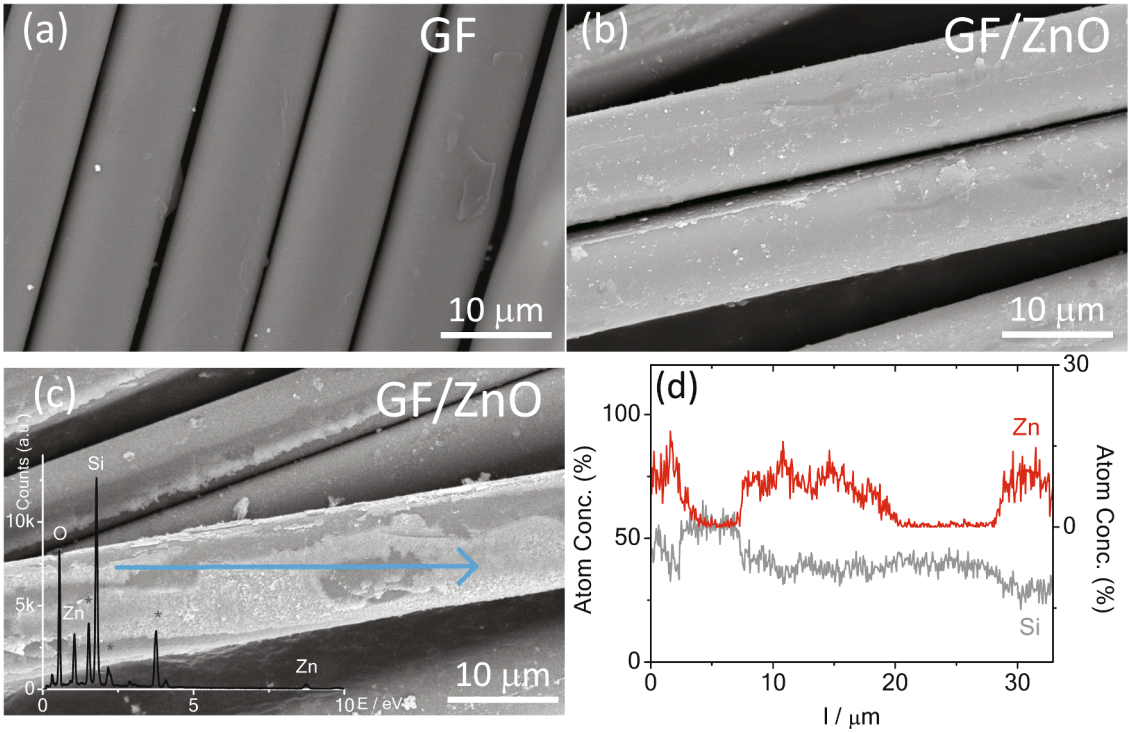

Fig. 7. SEM images of (a) GF, (b) GF/ZnO and (c) scratched area with line scan (blue arrow) and EDS spectra (Inset) and (d) plot of the atomic concentration of zinc (Zn) and silicon (Si), along the line scan. (* in EDS spectra denotes other substrate and/or conductive coating elements).

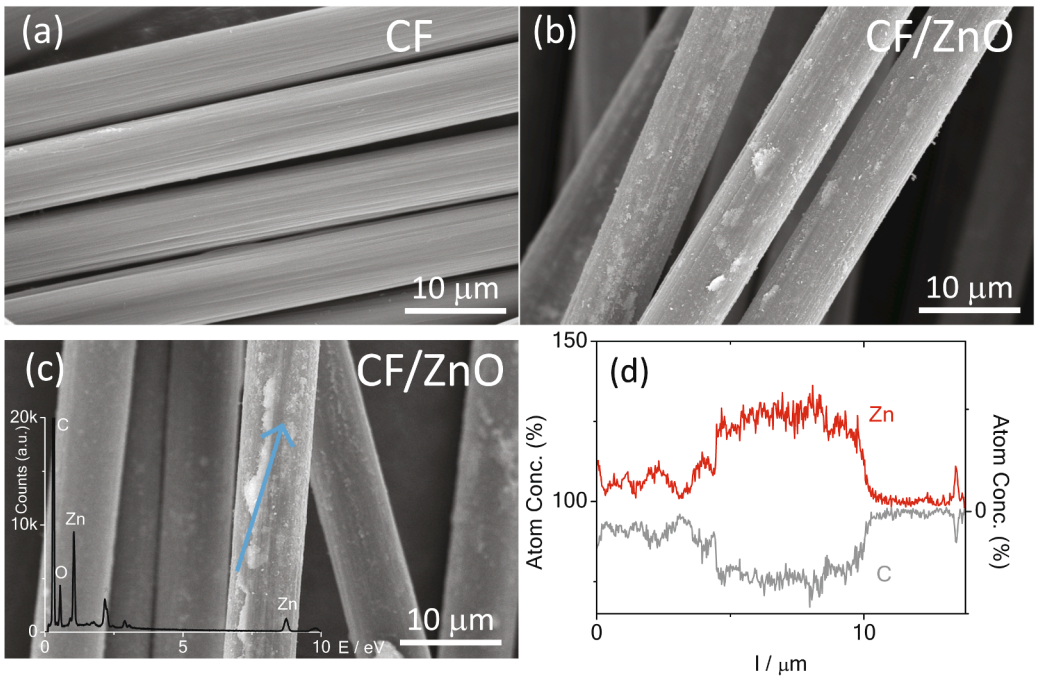

Fig. 8. SEM images of (a) CF, (b) CF/ZnO and (c) scratched area with line scan (blue arrow) and EDS spectra (Inset) and (d) plot of the atomic concentration of zinc (Zn) and carbon (C), along the line scan. (* in EDS spectra denotes other substrate and/or conductive coating elements).

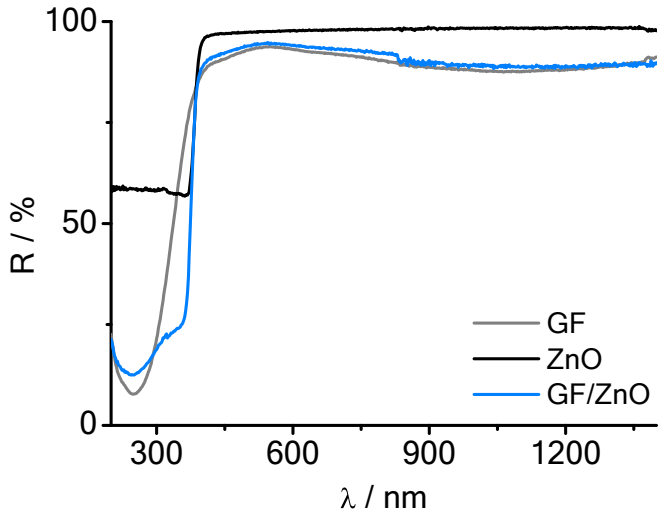

Fig. 9. Diffuse reflectance spectra for the GF/ZnO modified fibres and comparison with clean GF and pristine ZnO NP.

ZnO on GF (ESI, Figure S13b), probably due to the lower amount of NP immobilised.

Regarding the amount of ZnO NP immobilised on the fibres surface by the one pot *in situ* methodology used in this study, the AAS analysis allowed the quantification of ZnO on the CF/ZnO and GF/ZnO composites. On CF, a higher amount (18 mg/g) of ZnO NP was immobilised than on GF (15 mg/g), which may result from the more favourable interaction between ZnO and the carbon surface groups than with those of glass. This will have impact on the photocatalytic performance of the composite materials due to the distinct amount of catalyst available for the degradation of pollutants (4.5 and 3.8 mg in CF/ZnO and GF/ZnO, respectively), as compared with the 20.0 mg used as powder. This will be discussed in the next section.

3.4. Photocatalytic response of composite materials

Once immobilised on fibres by *in situ* methodologies, the composite CF/ZnO exhibits good photocatalytic response. In fact, DCF was successfully removed within 75 min under UV radiation, Fig. 10(a). Although the GF/ZnO shows lower photocatalytic response, it also allows the degradation of DCF and its degradation products in a higher extent than that of photolysis, Fig. 10(a). This behaviour may arise from (i) distinct amount of catalyst NP immobilised on CF and GF (4.5 and 3.8 mg) and (ii) beneficial effect of the combination of ZnO NP with the carbon material [3]. In fact, the coupling between carbon materials and ZnO has been reported to improve its activity by acting as electron scavenger and therefore decrease the e^-/h^+ recombination. Higher efficiency of carrier transport has been found, for example, in graphene oxide/ZnO nanocomposites and N-doped carbon nanotubes/ZnO [41,53].

Under visible radiation, GF/ZnO sample show a response comparable with that of photolysis, as illustrated in Fig. 10(b) for t = 90 min whereas CF/ZnO displayed a slightly better response.

In the case of DCF degradation, CF/ZnO was the best photocatalyst and the best response was obtained under UV light, for a short time.

A similarly behaviour was obtained for the CMZ photocatalytic degradation. The CF/ZnO composite exhibits the best response with the 100 % of CMZ successfully removed within 45 min under UV radiation, Fig. 11(a). GF/ZnO sample show an improvement of the photocatalytic activity of only ca. 6 % as compared with photolysis, Fig. 11(b). As mentioned above, this reflects not only the beneficial effect of the combination of carbon materials with the catalyst, but also the higher amount of catalyst immobilised on the CF/ZnO sample. Also important is the degradation efficiency of such composite as compared with pristine ZnO catalyst. Although distinct amount of catalyst is present in the photocatalytic assay (4.5 and 20.0 mg of ZnO for CF/ZnO and ZnO, respectively), both enable the complete removal of CMZ under UV radiation in a short period of irradiation time (60 min). That behaviour was also confirmed under visible radiation, Fig. 12.

Thus, the CF/ZnO modified fibres have been carried further for the CMZ photodegradation study under visible light irradiation. In Fig. 12 is illustrated the time profile for the CF/ZnO and its comparison with those

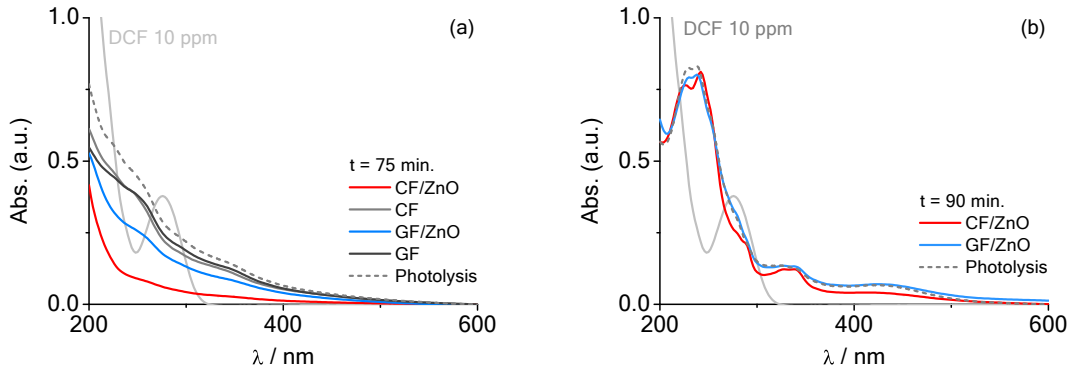

Fig. 10. UV–vis spectra for DCF degradation under (a) UV and (b) visible light irradiation using ZnO NP immobilised on CF and GF; comparison with photolysis.

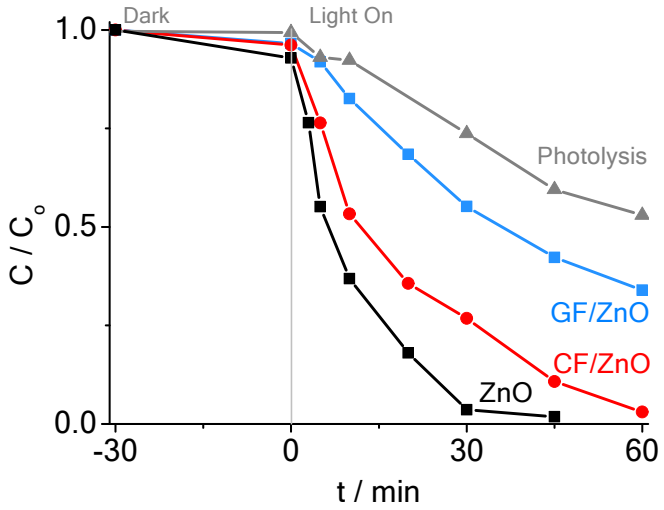

Fig. 11. Time profiles for the degradation of CMZ using modified fibres under UV light irradiation using carbon fibres: CF/ZnO and glass fibres: GF/ZnO, and comparison with ZnO NP suspension and photolysis.

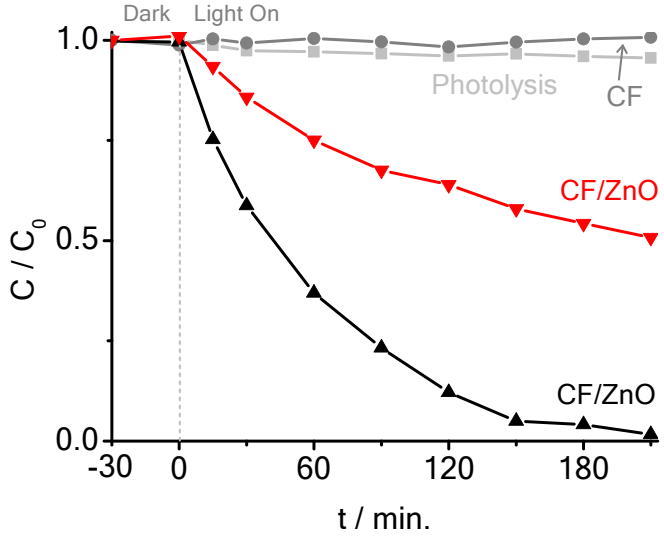

Fig. 12. Time profile for the CMZ degradation using CF/ZnO under visible light irradiation and comparison with pure ZnO NP, clean CF and photolysis.

for ZnO NP and photolysis.

The pristine CF and GF responses (not shown) coincide with that of photolysis indicating that the fibres by themselves do not take part in the photocatalytic degradation. In the presence of the catalyst, and highlighting the considerable smaller amount of NP immobilised on the surface of the fibres (4.5 mg) than the powder ZnO particles (20.0 mg) used in suspension, the composite exhibits promising results since it allows the degradation of ca. 50 % of the CMZ within 210 min, which is about 50 % of that attainable. The CF/ZnO composite maintains its activity with 80 % efficiency up to 3 reutilisation cycles. Although the obscuring effect of the black fibres may contribute to the current result, the photodegradation achieved is comparable to the performance of 2D layered titanium carbide materials under low frequency sonocatalytic conditions but requiring lower amount of catalyst and no other specialised equipment other than the visible light irradiation [11]. In fact, CF/ZnO enable the degradation of twice the expected amount of CMZ which may be due to the synergistic effect of combining carbon materials with the catalyst, mentioned above, and to the high photoactive surface area exposed during the photocatalytic degradation due to the limited aggregation of the nanocatalyst when immobilised on the fibres surface.

4. Conclusions

Crystalline ZnO nanocatalysts, both pure and doped with 1 % and 3 % manganese (Mn), were synthesized, showing a trend of decreasing particle size with increasing Mn content. The incorporation of Mn into ZnO extended its light absorption capabilities into the visible range without altering the material's bandgap energy. This modification did not result in an improvement in photocatalytic activity when compared to the undoped ZnO. The pristine ZnO nanoparticles (NPs), which showed superior efficiency towards the degradation of DCF and CMZ, were selected for creating composite materials with fiber substrates.

The successful modification of the fibers surface was confirmed by DRS and FTIR techniques, which identified ZnO-related absorption bands on both glass fiber (GF)/ZnO and carbon fiber (CF)/ZnO composites. Those results were further corroborated by SEM and EDS analyses, with the ZnO loading on GF and CF quantified by AAS as 15 mg/g and 18 mg/g, respectively.

The best response towards the degradation of the pollutants was retrieved by the carbon fibres-based composite due to the concomitant effect of the higher amount of nanocatalyst immobilised on CF (than on GF) and the synergistic effect of combining the ZnO catalyst with the carbon material.

Under UV light, the CF/ZnO composite showed enhanced efficiency in degrading DCF and achieving complete removal of CMZ. Despite a lower amount of catalyst used on the composite (4.5 mg) compared to the ZnO powder (20.0 mg), the degradation performance for CMZ was comparable within 1 h under UV radiation, which can be attributed to the stable immobilisation and dispersity of the catalyst on the CF surface.

Remarkably, using only a quarter of the catalyst amount compared to the ZnO powder and despite the potential shielding effect of CF, the CF/

ZnO composite managed to remove 50 % of CMZ within 3.5 h under the more cost-effective visible light, showcasing the composite's excellent photocatalytic capabilities.

CRediT authorship contribution statement

Inês V. Ferreira: Investigation, Formal analysis. **Nuno R. Neng:** Resources, Investigation, Formal analysis. **Olinda C. Monteiro:** Writing – review & editing, Supervision, Resources, Methodology, Conceptualization. **Virgínia C. Ferreira:** Investigation, Formal analysis.

Declaration of competing interest

The authors declare that they have no known competing financial interests or personal relationships that could have appeared to influence the work reported in this paper.

Data availability

Data will be made available on request.

Acknowledgements

This work was funded by Fundação para a Ciência e a Tecnologia (FCT) through projects UIDB/00100/2020, UIDP/00100/2020 for Centro de Química Estrutural (CQE) and LA/P/0056/2020 for Institute of Molecular Sciences (IMS). V.C. Ferreira and N.R. Neng acknowledge the financial support from FCT, DL 57/2016/CP1479/CT0049 and 57/2016/CP1479/CT0048 contracts.

Appendix A. Supplementary data

Supplementary data to this article can be found online at https://doi.org/10.1016/j.jphotochem.2024.115653.

References

[1] X. Yang, D. Wang, Photocatalysis: from fundamental principles to materials and applications, ACS Appl. Energy Mater. 1 (2018) 6657–6693, https://doi.org/10.1021/acsaem.8b01345.
[2] E.Y. Shaba, J.O. Jacob, J.O. Tijani, M.A.T. Suleiman, A critical review of synthesis parameters affecting the properties of zinc oxide nanoparticle and its application in wastewater treatment, Appl Water Sci 11 (2021), https://doi.org/10.1007/s13201-021-01370-z.
[3] C.B. Ong, L.Y. Ng, A.W. Mohammad, A review of ZnO nanoparticles as solar photocatalysts: Synthesis, mechanisms and applications, Renew. Sustain. Energy Rev. 81 (2018) 536–551, https://doi.org/10.1016/j.rser.2017.08.020.
[4] F. Achouri, S. Corbel, L. Balan, K. Mozet, E. Girot, G. Medjahdi, M.B. Said, A. Ghrabi, R. Schneider, Porous Mn-Doped ZnO Nanoparticles for Enhanced Solar and Visible Light Photocatalysis, Mater. Des. 101 (2016) 309–316, https://doi.org/10.1016/j.matdes.2016.04.015.
[5] M.A. Qamar, M. Javed, S. Shahid, Designing and investigation of enhanced photocatalytic and antibacterial properties of 3d (Fe Co, Ni, Mn and Cr) metal-doped zinc oxide nanoparticles, Opt. Mater. 126 (2022) 112211, https://doi.org/10.1016/j.optmat.2022.112211.
[6] B.G. Shohany, A.K. Zak, Doped ZnO nanostructures with selected elements - Structural, morphology and optical properties: A review, Ceram. Int. 46 (2020) 5507–5520, https://doi.org/10.1016/j.ceramint.2019.11.051.
[7] V.C. Ferreira, M.C. Neves, A.R. Hillman, O.C. Monteiro, Novel one-pot synthesis and sensitisation of new BiOCl-Bi_2S_3 nanostructures from DES medium displaying high photocatalytic activity, RSC Adv. 6 (2016) 77329–77339, https://doi.org/10.1039/c6ra14474h.
[8] C. Tang, C. Wang, F. Su, C. Zang, Y. Yang, Z. Zong, Y. Zhang, Controlled synthesis of urchin-like Bi_2S_3 via hydrothermal method, Solid State Sci. 12 (2010) 1352–1356, https://doi.org/10.1016/j.solidstatesciences.2010.05.007.
[9] V.C. Ferreira, W.R. Wise, O.C. Monteiro, Comparative study of powder and cotton-supported BiOCl particles on the photocatalytic degradation of industrial pollutants, Ceramics International 46 (2020) 27508–27516. (https://doi.org/10.1016/j.ceramint.2020.07.240).
[10] X. Yang, S. Sun, J. Cui, M. Yang, Q. Yang, P. Xiao, S. Liang, One-pot construction of robust BiOCl/ZnO p–n heterojunctions with semi-coherent interfaces toward improving charge separation for photodegradation enhancement, Nanoscale, Advances 3 (2021) 4851–4857, https://doi.org/10.1039/D1NA00396H.
[11] S. Kim, S.-N. Nam, C.M. Park, M. Jang, N. Taheri-Qazvini, Y. Yoon, Effect of single and multilayered Ti_3C_2TX MXene as a catalyst and adsorbent on enhanced sonodegradation of diclofenac and verapamil, J. Hazard. Mater. 426 (2022) 128120, https://doi.org/10.1016/j.jhazmat.2021.128120.
[12] L. Tang, J.-J. Wang, C.-T. Jia, G.-X. Lv, G. Xu, W.-T. Li, L. Wang, J.-Y. Zhang, M.-H. Wu, Simulated solar driven catalytic degradation of psychiatric drug carbamazepine with binary $BiVO_4$ heterostructures sensitized by graphene quantum dots, Appl Catal B 205 (2017) 587–596, https://doi.org/10.1016/j.apcatb.2016.10.067.
[13] K. Qi, B. Cheng, J. Yu, W. Ho, Review on the improvement of the photocatalytic and antibacterial activities of ZnO, J. Alloy. Compd. 727 (2017) 792–820, https://doi.org/10.1016/j.jallcom.2017.08.142.
[14] S. Kumar, A. Kumar, A. Kumar, V. Krishnan, Nanoscale zinc oxide based heterojunctions as visible light active photocatalysts for hydrogen energy and environmental remediation, Catal. Rev. 62 (2020) 346–405, https://doi.org/10.1080/01614940.2019.1684649.
[15] Y. Lu, Y. Lin, T. Xie, S. Shi, H. Fan, D. Wang, Enhancement of visible-light-driven photoresponse of Mn/ZnO system: photogenerated charge transfer properties and photocatalytic activity, Nanoscale 4 (2012) 6393–6400, https://doi.org/10.1039/c2nr31671d.
[16] S.C.A. Sousa, J.C. Cardoso, O.C. Monteiro, Improved performance of titanate nanostructures for manganese adsorption and posterior pollutants photocatalytic degradation, J. Photochem. Photobiol. A Chem. 378 (2019) 9–16, https://doi.org/10.1016/j.jphotochem.2019.04.009.
[17] M. Shatnawi, A.M. Alsmadi, I. Bsoul, B. Salameh, M. Mathai, G. Alnawashi, G. M. Alzoubi, F. Al-Dweri, M.S. Bawa'aneh, Influence of Mn doping on the magnetic and optical properties of ZnO nanocrystalline particles, Results Phys. 6 (2016) 1064–1071, https://doi.org/10.1016/j.rinp.2016.11.041.
[18] R. Khalid, A.N. Alhazaa, M.A.M. Khan, Synthesis, characterization and properties of Mn-doped ZnO nanoparticles, Appl. Phys. A 124 (2018) 536, https://doi.org/10.1007/s00339-018-1934-5.
[19] A. Wang, Z. Zheng, H. Wang, Y. Chen, C. Luo, D. Liang, B. Hu, R. Qiu, K. Yan, 3D hierarchical H_2-reduced Mn-doped CeO_2 microflowers assembled from nanotubes as a high-performance Fenton-like photocatalyst for tetracycline antibiotics degradation, Appl Catal B 277 (2020) 119171, https://doi.org/10.1016/j.apcatb.2020.119171.
[20] H. Wang, Q. Gao, H. Li, H. Wang, One-step template-free synthesis of Mn(II)-doped TiO2 hierarchical microspheres with unique radiating fibrous structure for efficient Fenton degradation, Mater. Res. Bull. 118 (2019) 110508, https://doi.org/10.1016/j.materresbull.2019.110508.
[21] B. Barrocas, L.D. Chiavassa, M. Conceição Oliveira, O.C. Monteiro, Impact of Fe, Mn co-doping in titanate nanowires photocatalytic performance for emergent organic pollutants removal, Chemosphere 250 (2020) 126240, https://doi.org/10.1016/j.chemosphere.2020.126240.
[22] Y. Wang, X. Hao, Z. Wang, M. Dong, L. Cui, Facile fabrication of Mn2+-doped ZnO photocatalysts by electrospinning, R. Soc. Open Sci. 7 (2020) 191050, https://doi.org/10.1098/rsos.191050.
[23] M.A. Adnan, N.M. Julkapli, S.B. Hamid, Review on ZnO hybrid photocatalyst: impact on photocatalytic activities of water pollutant degradation, Rev. Inorg. Chem. 36 (2016) 77–104, https://doi.org/10.1515/revic-2015-0015.
[24] A. Das, P.M. Kumar, M. Bhagavathiachari, R.G. Nair, Hierarchical ZnO-TiO_2 nanoheterojunction: A strategy driven approach to boost the photocatalytic performance through the synergy of improved surface area and interfacial charge transport, Appl. Surf. Sci. 534 (2020) 147321, https://doi.org/10.1016/j.apsusc.2020.147321.
[25] X. Tang, X. Yan, Dip-coating for fibrous materials: mechanism, methods and applications, J. Sol-Gel Sci. Technol. 81 (2017) 378–404, https://doi.org/10.1007/s10971-016-4197-7.
[26] Z. Han, V. Chang, L. Zhang, M. Tse, O. Tan, L. Hildemann, Preparation of TiO_2-Coated Polyester Fiber Filter by Spray-Coating and Its Photocatalytic Degradation of Gaseous Formaldehyde, Aerosol Air Qual. Res. 12 (2012) 1327–1335, https://doi.org/10.4209/aaqr.2012.05.0114.
[27] S. Lee, D. Kang, S. Jeong, H. Do, J.H. Kim, Photocatalytic Degradation of Rhodamine B Dye by TiO_2 and Gold Nanoparticles Supported on a Floating Porous Polydimethylsiloxane Sponge under Ultraviolet and Visible Light Irradiation, ACS Omega 5 (2020) 4233–4241, https://doi.org/10.1021/acsomega.9b04127.
[28] H. Chawla, S. Garg, P.P. Ingole, A. Chandra, Immobilization of Photocatalytic Material on the Suitable Substrate, in: S. Garg, A. Chandra (Eds.), Green Photocatalytic Semiconductors, Green Chemistry and Sustainable Technology. Springer, Cham, 2022, https://doi.org/10.1007/978-3-030-77371-7_15.
[29] M. Franco, O. Marin, N. Vega, M. Tirado, M. Tereschuk, D. Comedi, Surface nanostructuration of ZnO and ZnO: Cd sub-microstructures and their use as suspended and immobilized photocatalysts for rapid degradation of methylene blue, Mater. Lett. 311 (2022) 131634, https://doi.org/10.1016/j.matlet.2021.131634.
[30] J. Kim, M. Joshi, J. Lee, C. Park, C. Kim, Polydopamine-assisted immobilization of hierarchical zinc oxide nanostructures on electrospun nanofibrous membrane for photocatalysis and antimicrobial activity, J. Colloid Interface Sci. 513 (2018) 566–574, https://doi.org/10.1016/j.jcis.2017.11.061.
[31] V.C. Ferreira, A.J. Goddard, O.C. Monteiro, Cotton supported bismuthoxychloride and titanium dioxide: synthesis, characterisation and photocatalytic performance towards naphthol blue black dye degradation, J. Photochem. Photobiol. A Chem. 357 (2018) 201–212, https://doi.org/10.1016/j.jphotochem.2018.02.032.
[32] S. Deebansok, T. Amornsakchai, P. Sae-ear, P. Siriphannon, S. Smith, Sphere-like and flake-like ZnO immobilized on pineapple leaf fibers as easy-to-recover photocatalyst for the degradation of congo red, J. Environ. Chem. Eng. 9 (2021) 104746, https://doi.org/10.1016/j.jece.2020.104746.

[33] B.T. Barrocas, O.C. Monteiro, M.R. Nunes, A.J. Silvestre, Influence of Re and Ru doping on the structural, optical and photocatalytic properties of nanocrystalline TiO_2, SN Appl. Sci. 1 (2019) 556, https://doi.org/10.1007/s42452-019-0567-4.
[34] R. Ullah, J. Dutta, Photocatalytic degradation of organic dyes with manganese-doped ZnO nanoparticles, J. Hazard. Mater. 156 (2008) 194–200, https://doi.org/10.1016/j.jhazmat.2007.12.033.
[35] P. Zhang, X. Li, Q. Zhao, S. Liu, Synthesis and optical property of one-dimensional spinel $ZnMn_2O_4$ nanorods, Nanoscale Res. Lett. 6 (2011) 323, https://doi.org/10.1186/1556-276X-6-323.
[36] M. Imran, D.H. Kim, W.A. Al-Masry, A. Mahmooda, A. Hassan, S. Haider, S. M. Ramay, Manganese-, cobalt-, and zinc-based mixed-oxide spinels as novel catalysts for the chemical recycling of poly(ethylene terephthalate) via glycolysis, Polym. Degrad. Stab. 98 (2013) 904–915, https://doi.org/10.1016/j.polymdegradstab.2013.01.007.
[37] Z.R. Khan, M. Shkir, V. Ganesh, I.S. Yahia, S. Al-Faify, A facile microwave-assisted synthesis of novel $ZnMn_2O_4$ nanoparticles and their structural, morphological, optical, surface area, and dielectric studies, Indian J. Phys. 95 (2021) 43–49, https://doi.org/10.1007/s12648-020-01695-6.
[38] A. Toufiq, R. Hussain, A. Shah, A. Mahmood, A. Rehman, A. Khan, S. Rahman, The influence of Mn doping on the structural and optical properties of ZnO nanostructures, Phys. B 604 (2021) 412731, https://doi.org/10.1016/j.physb.2020.412731.
[39] K. Samanta, S. Dussan, R.S. Katiyar, P. Bhattacharya, Structural and optical properties of nanocrystalline $Zn_{1-x}Mn_xO$, Appl. Phys. Lett. 90 (2007) 261903, https://doi.org/10.1063/1.2751593.
[40] T. Fukumura, Z.-W. Zin, A. Ohtomo, H. Koinuma, M. Kawasaki, An oxide-diluted magnetic semiconductor: Mn-doped ZnO, Appl. Phys. Lett. 75 (1999) 3366–3368, https://doi.org/10.1063/1.125353.
[41] D.A. Giannakoudakis, N. Farahmand, D. Łomot, K. Sobczak, T.J. Bandosz, J. C. Colmenares, Ultrasound-activated TiO_2/GO-based bifunctional photoreactive adsorbents for detoxification of chemical warfare agent surrogate vapors, Chem. Eng. J. 395 (2020) 125099, https://doi.org/10.1016/j.cej.2020.125099.
[42] M.J. Chithra, M. Sathya, K. Pushpanathan, Effect of PH on Crystal Size and Photoluminescence Property of ZnO Nanoparticles Prepared by Chemical Precipitation Method, Acta Metallurgica Sinica (english Letters) 28 (2015) 394–404, https://doi.org/10.1007/s40195-015-0218-8.
[43] M.L. Silva-Neto, M.C.A. Oliveira, T.C. Dominguez, R.E.M. Lins, N. Rakov, C. B. Araújo, L.S. Menezes, H.P. Oliveira, A.S.L. Gomes, UV Random Laser Emission from Flexible ZnO-Ag-Enriched Electrospun Cellulose Acetate Fiber Matrix, Sci. Rep. 9 (2019) 11765, https://doi.org/10.1038/s41598-019-48056-w.
[44] S. Yedurkar, C. Maurya, P. Mahanwar, Biosynthesis of Zinc Oxide Nanoparticles Using Ixora Coccinea Leaf Extract - A Green Approach, Open Journal of Synthesis Theory and Applications 5 (2016) 1–14, https://doi.org/10.4236/ojsta.2016.51001.
[45] S.D. Birajdar, R.C. Alange, S.D. More, V.D. Murumkar, K.M. Jadhav, Sol-gel auto combustion synthesis, structural and magnetic properties of Mn doped ZnO nanoparticles, Procedia Manufacturing 20 (2018) 174–180, https://doi.org/10.1016/j.promfg.2018.02.025.
[46] E. Moctezuma, E. Leyva, C. Lara-Pérez, S. Noriega, A. Martinez-Richa, TiO_2 Photocatalytic Degradation of Diclofenac: Intermediates and Total Reaction Mechanism, Top. Catal. 63 (2020) 601–615, https://doi.org/10.1007/s11244-020-01262-7.
[47] L. Bo, K. He, N. Tan, B. Gao, Q. Feng, J. Liu, L. Wang, Photocatalytic oxidation of trace carbamazepine in aqueous solution by visible-light-driven $ZnIn_2S_4$: Performance and mechanism, J. Environ. Manage. 190 (2017) 259–265, https://doi.org/10.1016/j.jenvman.2016.12.050.
[48] A. Jelic, I. Michael, A. Achilleos, E. Hapeshi, D. Lambropoulou, S. Perez, M. Petrovic, D. Fatta-Kassinos, D. Barcelo, Transformation products and reaction pathways of carbamazepine during photocatalytic and sonophotocatalytic treatment, J. Hazard. Mater. 263 (2013) 177–186, https://doi.org/10.1016/j.jhazmat.2013.07.068.
[49] S. Begum, M. Ahmaruzzaman, CTAB and SDS assisted facile fabrication of SnO_2 nanoparticles for effective degradation of carbamazepine from aqueous phase: A systematic and comparative study of their degradation performance, Water Res. 129 (2018) 470–485, https://doi.org/10.1016/j.watres.2017.11.031.
[50] V. Ţucureanu, A. Matei, A. Avram, FTIR Spectroscopy for Carbon Family Study, Crit. Rev. Anal. Chem. 46 (2016) 502–520, https://doi.org/10.1080/10408347.2016.1157013.
[51] B. Xu, J. Long, G. Xu, J. Yang, Y. Liang, J. Hu, Facile fabrication of superhydrophobic and superoleophilic glass-fiber fabric for water-in-oil emulsion separation, Text. Res. J. 89 (2019) 2674–2681, https://doi.org/10.1177/0040517518801189.
[52] A.M. Mhatre, S. Chappa, S. Ojha, A.K. Pandey, Functionalized glass fiber membrane for extraction of iodine species, Sep. Sci. Technol. 54 (2019) 1469–1477, https://doi.org/10.1080/01496395.2018.1520729.
[53] M.J. Sampaio, R.R. Bacsa, A. Benyounes, R. Axet, P. Serp, C.G. Silva, A.M.T. Silva, J.L. Faria, Synergistic effect between carbon nanomaterials and ZnO for photocatalytic water decontamination, J. Catal. 331 (2015) 172–180, https://doi.org/10.1016/j.jcat.2015.08.011.